EES Batteries

ROYAL SOCIETY OF CHEMISTRY

PAPER

View Article Online
View Journal | View Issue

Cite this: *EES Batteries*, 2025, **1**, 1208

Sensor-less estimation of battery temperature through impedance-based diagnostics and application of DRT

Danial Sarwar, * Oliver Curnick and Tazdin Amietszajew

Temperature has a substantial influence on the overall safety and performance of Lithium-ion batteries. Given the constraints of onboard thermal sensors and their inability to accurately measure internal cell temperature, a reliable temperature estimation has become a crucial aspect of battery state monitoring. This study exploits the temperature-sensitivity of electrochemical impedance spectroscopy (EIS) measurements to propose a sensor-less method to accurately estimate the internal temperature of commercial lithium-ion batteries. The presented study explores the reliability and limitations of the EIS-based method *via* a comparative analysis on two different cell types, *i.e.*, high impedance (cylindrical 5 Ah) and low impedance (pouch 40 Ah) cells, over a range of multiple SOCs and temperatures. Furthermore, a novel approach of distribution of relaxation times (DRT) to extract the temperature-sensitive features from EIS data is also investigated. The results show that method is capable of estimating the internal temperature of high-energy cylindrical cells with an accuracy of $\pm$0.41 °C, and high power pouch cells with an accuracy of $\pm$2.22 °C over the entire range of tested SOCs. Overall, the Arrhenius model (for both cell types) represents a good fit for all the extracted features with $R^2 > 0.9$. Charge transfer resistance (R_{CT}) was found to be the most significant predictor for cylindrical cells and ohmic resistance (R_{ohm}) for pouch cells. Furthermore, DRT peak heights can serve as a thermally sensitive feature for cell temperature estimation with good accuracy (typically <3 °C, though dependent on cell impedance response profile), and potential for broader applicability than features derived from equivalent circuit modelling. The study illustrates the opportunities and challenges associated with implementing impedance-based temperature estimation methodologies.

Received 13th May 2025,
Accepted 24th June 2025

DOI: 10.1039/d5eb00092k

rsc.li/EESBatteries

Broader context

The safe operation and performance optimization of lithium-ion batteries are crucial for their application in consumer electronics, electric vehicles, and renewable energy storage systems. Conventional methods of monitoring battery thermal state rely on temperature sensors, which present challenges such as surface-only data collection, complex wiring, and added weight. These limitations have driven the search for more efficient methods. Recent advancements in Electrochemical Impedance Spectroscopy (EIS) offer a quick and reliable technique for estimating battery temperature without complex thermal models. Our study introduces a sensor-less approach using EIS to infer battery temperature, addressing the challenges of conventional methods. By performing a comparative evaluation of relevant commercially available high energy and high power cells across various temperatures and states of charge (SOCs), we highlighted the strengths and limitations of this method. Due to limited research on the Distribution of Relaxation Times (DRT) method, we explored its potential to estimate battery temperature by separating time constants and extracting temperature-dependent features. The method demonstrated higher estimation accuracy for high energy cells, highlighting its commercial potential. Our findings enhance battery safety and performance, supporting the development of efficient and reliable energy storage solutions, and paving the way for future innovations in battery monitoring technologies.

1. Introduction

Lithium-ion battery technology has proven to be an ideal candidate for an alternative and sustainable energy storage, especially in the area of mobility.[1] Lithium-ion batteries (LIBs), owing to their high gravimetric/volumetric energy density,[2] low self-discharge, longer cycle life, and high output voltage (~4.2 V), have eclipsed previously used rechargeable batteries and have been widely utilised in portable consumer products, EVs and grid storage.[3,4] Despite vast adoption, wider use of lithium-ion batteries (LIBs) is not without a challenge to meet the increasing market and consumer expectations for

Centre for E-Mobility and Clean Growth (CECG), Coventry University, Coventry CV1 2TL, UK. E-mail: danial.sarwar@coventry.ac.uk

high performance, safety and durability. To achieve this, it is imperative that the operating conditions of batteries are well monitored and controlled. One of the key functions of a battery management system (BMS) is temperature monitoring, as it has a major influence not only on battery performance and life, but may also induce safety failure, with Li-ion cells subject to severe temperature-dependent degradation and failure modes such as thermal runaway.[5–7] In the worst-case scenario, if the battery temperature exceeds the safety threshold, then thermal runaway may occur, accompanied by catastrophic failure and fire. Aside from severe scenarios, abnormal temperature changes could affect the overall performance and cycle life of the battery. Low temperatures could also drastically decline available battery power and energy due to sluggish electrochemical kinetics.[8] Fast charging at low temperatures could increase the risk of lithium plating, resulting in degradation of battery health.[1,9]

Traditionally, battery temperature is monitored using temperature sensors, such as thermocouples and thermistors, mounted externally to the cells. The actual internal temperature could differ from surface temperature during non-equilibrium conditions. This was demonstrated in our previous works,[10–12] where we implemented *in situ* thermal monitoring by embedding thermistors inside the pouch and cylindrical cells. Most importantly, it was found that the maximum core temperature exceeded the electrolyte stability limit under certain conditions. Various other studies also highlighted this by directly measuring internal temperature.[13–19] Thus, the approach of using surface-mounted physical sensors suffers from heat transfer delay, so relying only on surface data could cause ambiguity in identifying thermal failures. The method of embedding sensors into cells provides highly accurate and localised thermal data; however, implementation of this on a large scale could pose challenges, not least around the additional cost posed by the instrumentation. Additionally, ensuring long-term sensor stability and data reliability within the harsh electrochemical environment is still challenging, particularly in real-world battery systems that must operate varied duties under a range of environmental conditions over thousands of hours without extensive maintenance.

In practical applications, the number of thermal sensors is limited, *e.g.*, 10 sensors for 76 cells in Ford C-Max and 16 for 288 cells in the Chevy Volt[20,21] and 4 sensors in the early 24 kWh battery pack of Nissan leaf.[22] With such sensor-to-cell ratio, thermal information of each individual cell cannot be accessed, as it is impractical to use sensors for every cell owing to wiring harness complexity, cost and weight.[21] We propose to alleviate this issue by implementing a sensor-less approach, that could be utilized to infer the temperature of each cell solely based on measured electrical parameters.

Impedance-based cell state estimation has gained attention recently as a non-invasive and temperature-sensitive method. Such a technique could be utilised as either a stand-alone or a complementary approach beside a thermal sensor for reliable data acquisition. Various previous studies highlighted the potential of using impedance parameters extracted from EIS (electrochemical impedance spectroscopy) to infer battery temperature.[2,23–30] The impedance measured from EIS tests can be expressed in the form of a complex number encompassing real and imaginary parts, containing information pertaining to the amplitude and phase shift of the device's current response to a sinusoidal voltage stimulus. The pioneering work by Srinivasan *et al.*[23] quantised the monotonic relation between phase shift and battery temperature by keeping the frequency range of 40 Hz–100 Hz. Although the authors provided a theoretical basis of phase change to ionic conduction within SEI layer, the assumption of SEI stability could limit the estimation accuracy, as the SEI properties may vary under abusive or ageing conditions. A similar correlation was also studied by Schwarz *et al.*[31] Their work is commendable for its practical aspect, through the use of fixed frequency phase measurements rather than a full or range of EIS spectra. Therefore, reducing computational and hardware complexity making the approach attractive for automotive and stationary applications. On the contrary, some studies also made use of the real part[32] and imaginary part[29] of impedance to correlate with temperature. More detailed aspects of various studies utilising impedance to infer battery temperature can be found in review articles.[1,3]

In this study, a novel approach of employing distribution of relaxation times (DRT) for analytical treatment of EIS data is demonstrated for the estimation of battery temperature. Particular features from EIS and DRT are extracted and related to temperature based on their strong Arrhenius relation. Finally, we compare the estimation accuracy and evaluate the strengths and limitations of applying herein proposed methods, using two commercial cell types with different impedance ranges.

2. Methodology

2.1. Impedance-based temperature estimation

Electrochemical Impedance Spectroscopy (EIS) can be employed for sensor-less temperature estimation, under its ability to probe time-dependent processes (*e.g.* electron transfer in electrochemical reactions), whose time constants are temperature dependent. The relationship between reaction rate and associated temperature is governed by Arrhenius equation[7] as shown in eqn (1). Changes in internal cell dynamics due to temperature are reflected in the impedance response; thus, an intrinsic relationship can be developed between impedance and internal temperature.

$$\text{Rate constant} = A \cdot e^{-E_a/K_b T} \quad (1)$$

where; A is pre-exponential factor, E_a is activation energy, K_b is Boltzmann constant, and T is temperature.

In order to identify a reliable impedance-temperature relationship, it is crucial to identify and extract the inherent features exhibiting a strong correlation, whilst accounting for the effects of other factors (*e.g.* SOC) that influence the impedance response. Interpretation of impedance response to

facilitate temperature estimation remains a challenge, necessitating innovative approaches for improvement. Equivalent circuit modelling (ECM) utilises discrete circuit components that correspond to multiple physiochemical processes that are sensitive to temperature changes. To our best knowledge, there are limited studies available focusing on ECM-based features for temperature estimation. Instead, most studies relied on raw impedance data, including phase shift,[23,25,31] real/imaginary part[28,29,32,33] and intercept frequency.[2,26]

However, as the performance of LIB is governed by multiple electrochemical processes, contributions within EIS spectra are generally overlapped and thus cannot be distinguished unambiguously. Furthermore, ECM is dependent on the *a priori* knowledge of system response, requiring a suitable configuration that embodies the battery's internal dynamics,[34] which then needs to be adapted following a change in operating conditions. To overcome these issues, DRT is deployed here as a model-independent method. It allows for deconvolution of EIS spectra from frequency to time domain, where distinct time constants related to multiple processes can be discerned without making any assumptions regarding the number of processes or their time constants. Fundamentally, DRT makes use of the fact that complex impedance response for an electrochemical system can be modelled by an infinite series of resistive-capacitive elements as shown in eqn (2). The term within the integral mentioned in eqn (2) represents the differential contribution of a single R||C element to the total polarization, where $\gamma(\tau)$ is the ratio of ohmic resistance R to total polarization resistance. The DRT function is computed by discretizing the integral and taking only finite RC elements. Thus, the distribution curve is divided into a series of n parallel RC elements, ranging from time constants of τ_1 to τ_n. This interval is usually determined by the frequency span of available impedance data.

$$Z_{\mathrm{DRT}} = \int_{\tau_1}^{\tau_n} \frac{\gamma(\tau)}{1 + j\omega\tau} \mathrm{d}\tau \tag{2}$$

Therefore, DRT makes no *a priori* assumption for the number of processes and thus bypasses ECM-based ambiguity and can be utilised as a model-free approach.[35] Recently, DRT has been used to diagnose and separate degradation mechanisms in lithium-ion batteries.[36–38] However, the use of DRT in temperature estimation is still very limited.[30] This study thus utilises multiple features from EIS data, *i.e.*, raw data (phase), parameters from ECM, and peaks from the DRT to estimate cell temperature. A freely available online tool, *i.e.*, DRTtools developed by Wan *et al.*[39] was utilised for DRT analysis in this study. Furthermore, by performing a comparative study between two different cells, we evaluate the limitations of these methods over a range of temperatures, particularly at the higher end, owing to limited EIS accuracy for low-impedance cells.

2.2. Experimental

To perform a comparative sensor-less study, two distinct types of LIBs were evaluated with different ranges of impedance. The tested cells are commercially available LG-M50 (high impedance/high energy) cylindrical and SPIM11309102 (low impedance/high power) MGL-pouch cells. These particular pouch cells are intended for PHEV (plug-in hybrid electric vehicle) applications. Detailed cell specifications can be found in Table 1.

DC cycling and EIS measurements were performed using Biologic VMP3 potentiostat (EC-Lab® 11.54 software) with 5 A and 20 A boosters as required by the test's maximum current. To maintain temperature consistency, cells were kept inside thermally controlled chambers (Binder KB115). The cells were supplied new, purchased from the local distributor. Prior to the start of the EIS-temperature study, all cells underwent a preconditioning stage. The procedure is as follows: cells were subjected to 3 cycles of constant current charge/discharge at an ambient temperature of 25 °C. A current of 0.3C and 0.5C was used for cylindrical and pouch cells respectively, with a cut-off current of 0.05C during the constant voltage step.

Furthermore, for temperature estimation tests, a temperature range of 25 °C to 60 °C (tested at each 5 °C increment) was selected and cells were tested under 5 different SOCs, *i.e.*, 10%, 30%, 50%, 70%, and 90%. EIS measurements were performed in potentiostatic mode by applying a 10 mV AC excitation under a frequency range of 50 mHz–1 kHz with 12 points per decade on logarithmic scale. Before each temperature test, cells were kept at a constant temperature for about 5 hours to equilibrate. Cells were first charged to 90% SOC, followed by an EIS measurement. They were then discharged with a decrement of 20% before each subsequent EIS measure-

Table 1 Cells specification

	Cells tested	
Item	LG M50[40]	SPIM11309102-GL40[41]
Form factor	Cylindrical 21 700	Pouch 309 mm × 102 mm
Nominal capacity	4.85 Ah	40 Ah
Weight	68 g	730 g
DC-resistance (AC impedance at 1 kHz)	30 mΩ (≤25 mΩ)	≤1.4 mΩ (≤0.65 mΩ)
Standard charge rate	0.3C (1.45 A)	1C (40 A)
Voltage window	2.5 V–4.2 V	2.5 V–4.2 V
Chemistry	NMC811 (Li $(Ni_{0.84}Co_{0.10}Mn_{0.06})O_2$)/graphite–$SiO_x$	NMC[42]

ment until the SOC of 10% was achieved. To ensure equilibrium conditions, a rest period of 1 hour was provided before each EIS step.

3. Results and discussion

3.1. Preliminary characterisation of impedance features

The focus of this work is to identify the correlation between the features present in EIS data and temperature, and to investigate the dependence of this correlation on SOC. Full EIS spectra measured at multiple SOCs and temperature are shown in Fig. 1 and 2 for both cell types evaluated. Focusing on Nyquist plots in Fig. 1a and c, it can be observed that impedance response is weakly dependent on SOC in the range 30–90% and the high to mid-frequency region. However, it is highly affected under 10% SOC for both cell types, resulting in right shift of the Nyquist plot, particularly in the low-frequency region. At around 318 Hz and 4 Hz for cylindrical and pouch cells respectively, there is also a prominent shift (focusing on the zero-crossing), indicating an increase in ohmic resistance as the cell voltage is reduced.

An enlarged mid-frequency semicircle (related to charge transfer/interfacial processes) can be observed at 10% SOC for both cell types. This phenomenon can be explained in a way that during low SOCs, due to high lithiation of cathode, the cell experiences an increase in impedance. By comparing Nyquist plots for both cell types (Fig. 1(a) and (c)), the difference in impedance response is visible by the change in shape. This can be noticed by the disappearance of mid-semi circle for pouch cells, primarily because of their low impedance and the presence of inductive effects at high frequencies.

It can be argued that the charge transfer processes are more prominent in cylindrical cells compared to pouch cells

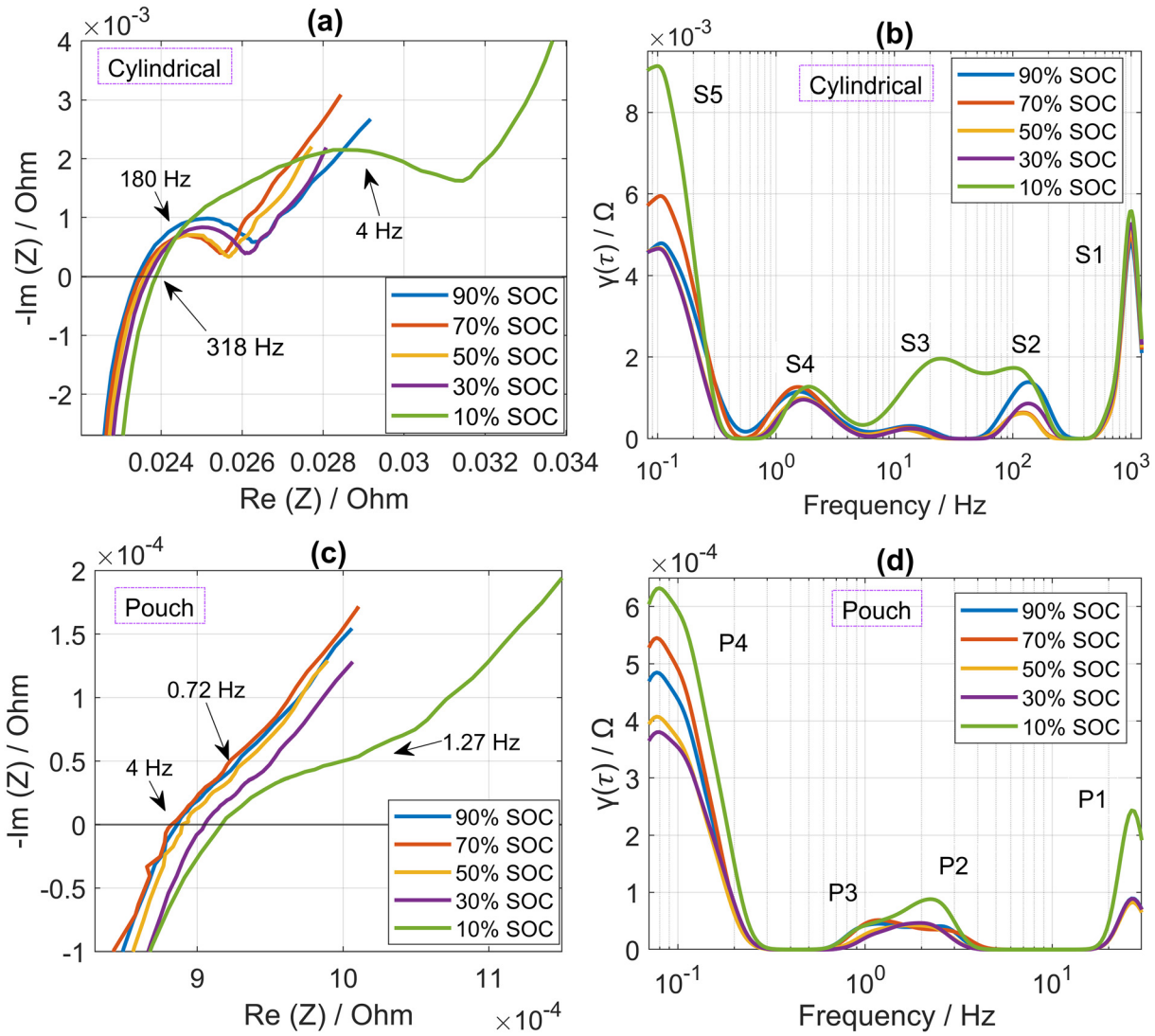

Fig. 1 Effect of SOC on impedance response for both cell types at 25 °C (a) and (b) EIS and DRT plot for cylindrical cells, (c) and (d) EIS and DRT plots for pouch cells.

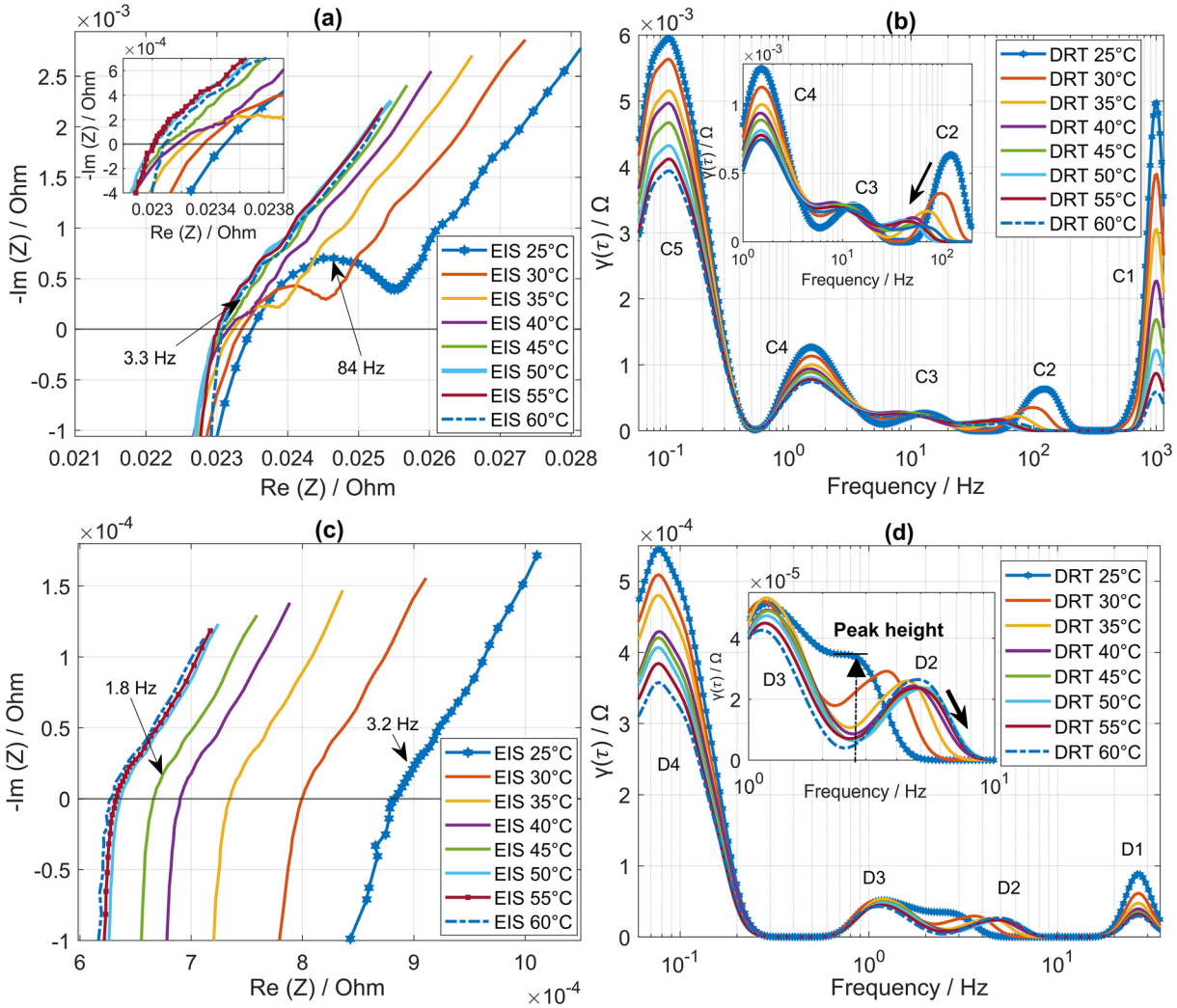

Fig. 2 Impedance response (Nyquist plot) and deconvolution of EIS (DRT) at multiple temperatures for both cell types indicating temperature dependence at SOC = 70%, (a) and (b) EIS and DRT for cylindrical cell, (c) and (d) EIS and DRT for pouch cell.

particularly for the cells tested here. One of the inherent drawbacks of relying solely on Nyquist-based analysis is its limited ability to resolve and quantify impedance losses arising from processes with similar time constants. It is thus challenging to identify overlapped time constants referring to each electrochemical process. An alternative technique for parameterization of EIS data is offered by DRT analysis, where polarization peaks related to each process can be identified, thus separating the individual electrochemical processes on a time scale.[43]

As shown in Fig. 1(b and d), DRT analysis was able to separate individual processes that were indistinguishable in Nyquist plots. Under identical test conditions, a higher number of peaks (S1–S5) can be observed for cylindrical cells than for pouch (P1–P4). The change in impedance response for 10% SOC is also visible in DRT, but with additional information. For both cylindrical and pouch cells, an extra peak, *i.e.*, S3 and P2 can be identified for 10% SOC as shown in Fig. 1(b and d), indicating that an additional process becomes dominant at low SOC. Particularly for pouch cells, as shown in Fig. 1(c and d), even with the suppressed semicircle (in the high to mid-frequency region) for higher SOCs, two distinct peaks (P2 and P3) can be identified in the DRT plot. Hence, it can be concluded that DRT played a vital role here in identifying particular features useful for temperature estimation.

The mid-frequency (1–100 Hz) peaks in DRT plots are usually associated with anodic/cathodic charge transfer and interfacial processes. Associating the peaks to specific processes remains a challenge in full-cell measurements, which, while representative of real-life scenarios, exhibit convoluted electrode phenomena. This is sometimes possible using half-cell impedance measurements, which allow for independent derivation of DRT spectra for each electrode. However, since detailed half-cell measurements are out of the scope of this study, we have ascribed DRT peaks to different processes based on previous studies reported in the literature.[43] As an

example, the peaks S1 and P1 could be ascribed to particle–particle and contact resistance. The frequency and amplitude of these peaks are invariant with SOC in the range of 30–90%. Furthermore, according to the kinetics of the electrochemical process the following peaks, *i.e.*, (S2, S3, S4), and (P2, P3) could be associated to interfacial and charge transfer processes. Due to the better representation of mid-frequency semi-circle for cylindrical cells, a better separation of these processes can be observed as compared to pouch cells. This is also in agreement with work done by Iurilli *et al.*,[43] who used a similar cylindrical cell to that used in this study. Based on their half-cell/full-cell analysis, they associated the peaks near 10^3 Hz with SEI and peaks in the range of 10^{-1}–10^2 Hz with anodic/cathodic charge transfer processes.

Furthermore, Fig. 2 illustrates the cell's impedance response across multiple temperatures. As expected, EIS response for both cell types (see Fig. 2(a and c)) showed a shift towards lower impedance as temperature increased. The reduction in ohmic resistance (R_{ohm}) could be the consequence of enhanced electrolyte conductivity with increasing temperature. Moreover, particularly for cylindrical cells (Fig. 2(a)), a decrease in charge transfer resistance (as indicated qualitatively by a reduction in the radius of the semicircle) can be observed due to faster kinetics at elevated temperatures. The semicircle could be related to interfacial and charge transfer characteristics, and thus with increasing temperature, *i.e.*, above 40 °C, the time constants related to internal processes become similar and difficult to distinguish. However, on the other hand, the diminishing of interfacial/charge transfer characteristics with increasing temperature is not prominent for pouch cells (see Fig. 2(c)). Due to the very low impedance of pouch cells, the time constants of respective charge transfer processes overlapped/merged with the diffusion tail and thus difficult to interpret. Thus, from a qualitative analysis perspective it can be argued that, for temperature estimation using the Nyquist plot, different features could be selected for each cell type. Hence, R_{CT} and R_{ohm} will be utilised here to infer battery temperature for cylindrical and pouch cells respectively. This will be further analysed by extracting individual circuit parameters using ECM in the next section.

The poorly resolved features in Nyquist representation were more apparent in DRT spectra (see Fig. 2(b and d)), where distinctive peaks related to interfacial/charge transfer characteristics could be observed, *i.e.*, Peaks C2–C4 and D2, D3 for cylindrical and pouch cells respectively. Thus, DRT appears useful for the derivation of temperature-dependent features by selecting the peaks that are highly temperature-sensitive. Two major temperature-dependent characteristics of peaks C2 and D2 can be identified, *i.e.*, shift in their time constants (τ) and change in their amplitudes, as indicated by arrows in Fig. 2(b and d) inserts. Additionally, it is important to note that shifts in particular time constants are the consequence of changes in electrochemical kinetics. This shift cannot be identified using the Nyquist plot, as an example, two frequencies (3.2 Hz and 1.8 Hz for 25 °C and 45 °C respectively) are pointed out manually at almost similar locations (see Fig. 2(c)). Due to faster kinetics, the positioning of particular τ changed and thus became more observable by the shift of D2 in the DRT plot towards higher frequencies. Based on these observations peak heights of C2 and D2 were utilised to evaluate an Arrhenius relation using DRT.

In addition to ECM and DRT-based temperature estimation, for comparison purposes, we have also considered extracting features from raw impedance data, *i.e.*, phase shift (φ). Fig. 3 illustrates the Bode plot at 70% SOC for both cell types. It can be observed from the inserts in Fig. 3(a and b), that variation of φ with temperature is most pronounced in the range of 10

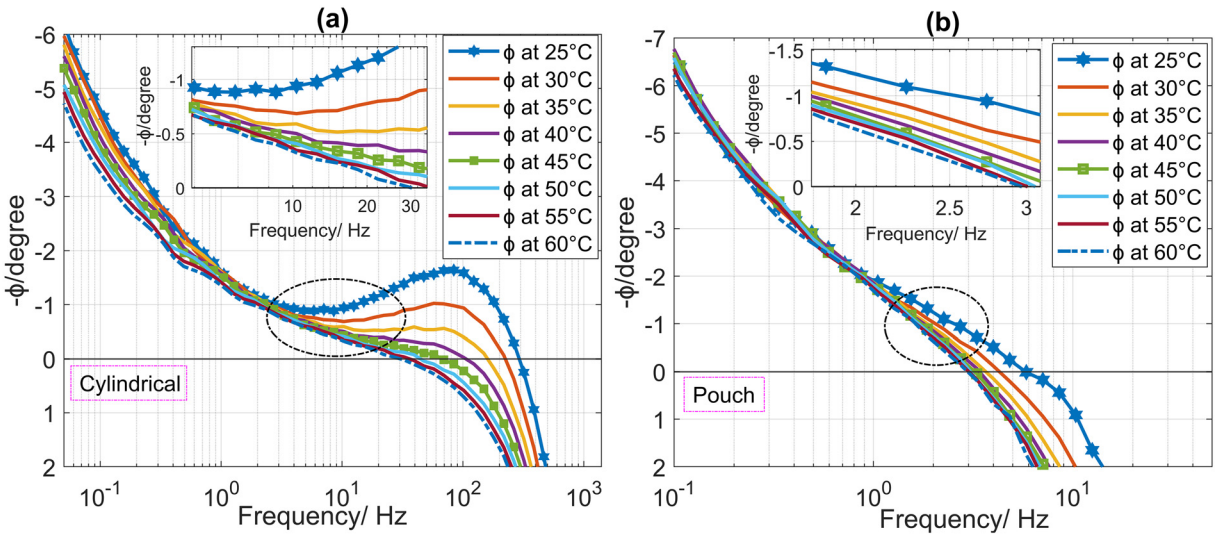

Fig. 3 Bode plot indicating phase shift at multiple temperatures under SOC = 70% (a) cylindrical cell phase difference and showing temperature dependence as an insert, (b) phase shift for pouch cell and an insert focusing on a particular frequency region for temperature dependence, as circled in the main figure.

Hz–35 Hz and 2 Hz–3 Hz for cylindrical and pouch cells, respectively. The temperature-sensitive window for pouch cell features is much smaller than for cylindrical cells. This difference could be due to a larger influence of inductive effects at high frequencies, resulting in masking of charge transfer/interfacial characteristics for pouch cells in the impedance response. A weak relationship can be observed in the low-frequency range for both cell types and hence can be excluded for temperature estimation. It is also important to highlight that the rate of change in phase with temperature ($\Delta\varphi/\Delta T$) tends to get smaller with increasing temperature, particularly above 45 °C for both cell types. As an example, in the case of cylindrical cells at 22 Hz (Fig. 3(a)), $\Delta\varphi/\Delta T$ between 25 °C to 45 °C is 0.047 per °C, however it is reduced to 0.011 per °C for the temperature range of 45 °C to 60 °C. A similar observation was also made by Srinivasan *et al.*[23] while testing at higher temperatures. Furthermore, in our study, this observation is also in line with a change in R_{ohm} (see Fig. 2(c)).

3.2. Feature-based Arrhenius relation

As discussed earlier, the correlation between impedance characteristics and temperature is not linear over the whole range of tested temperatures. In Fig. 4, we have illustrated this *via* an Arrhenius relation of peak heights from cylindrical (C2) and pouch (D2) cells with temperature. To transform the exponential function in eqn (1) to linear form, all the Arrhenius relations are plotted here by taking the logarithmic of impedance features. A monotonic relation can be observed with increasing temperature only up to 45 °C as highlighted in Fig. 4(a and b). This is similar for both cell types. The activation energy (E_a) in eqn (1) can be calculated by the slope of the Arrhenius relation. Thus, it can be argued that over a wider range of temperatures, there could be multiple activation energies due to varying impacts of temperatures on the cell. This was also observed by Spinner *et al.*,[29] who used imaginary impedance to build the Arrhenius relation over a wider temperature range of −10 °C to 95 °C, while utilising a secondary correlation trend to fit the temperatures above 60 °C, which suggests more than one activation energy in effect.

This is a consequence of parallel phenomena affecting the battery when operating at high temperatures, as seen in deviation from linear correlation above 45 °C in our study. Multiple parasitic electrochemical reactions can occur during elevated operating conditions, such as the growth and decomposition of solid electrolyte interface (SEI) and cathode materials, electrolyte degradation and transition metals dissolution, among mechanisms that are exacerbated due to high temperatures.[7] In our test setup, the influence of these processes could not be controlled; thus, we have restricted our subsequent analysis to a range of 25 °C to 45 °C.

Furthermore, as discussed earlier, three different impedance features were extracted here for temperature estimation, *i.e.*, (i) using ECM, (ii) DRT peak heights, and (iii) phase shift (extracted from raw data). By conducting a qualitative analysis of Nyquist plots for both cell types (see Fig. 2(a and c)), and given the absence of well-pronounced semicircles, a simple Randles circuit with a single RC component was used. The circuit configuration is shown in Fig. 5(a), and least-squares fitting was performed using the Z-View software.[44]

Interestingly, an inherent limitation of ECM fitting was observed here, particularly for pouch cells. The Nyquist plot for pouch cells does not exhibit distinguishable semicircles (interfacial/charge-transfer characteristics) in the mid-frequency region due to very low impedance. Despite the fitting errors being in an acceptable range (see table in Fig. 5(a)), a poor linear correlation between R_{CT} and the temperature was observed as shown in Fig. 5(b). This was the same for all tested SOCs except for 10% SOC, possibly due to a slight increase in impedance.

On the contrary, a satisfactory correlation (R_{CT} *versus* temperature) was found for cylindrical cells under all SOCs as shown in Fig. 6(a). It can also be noticed that there is an

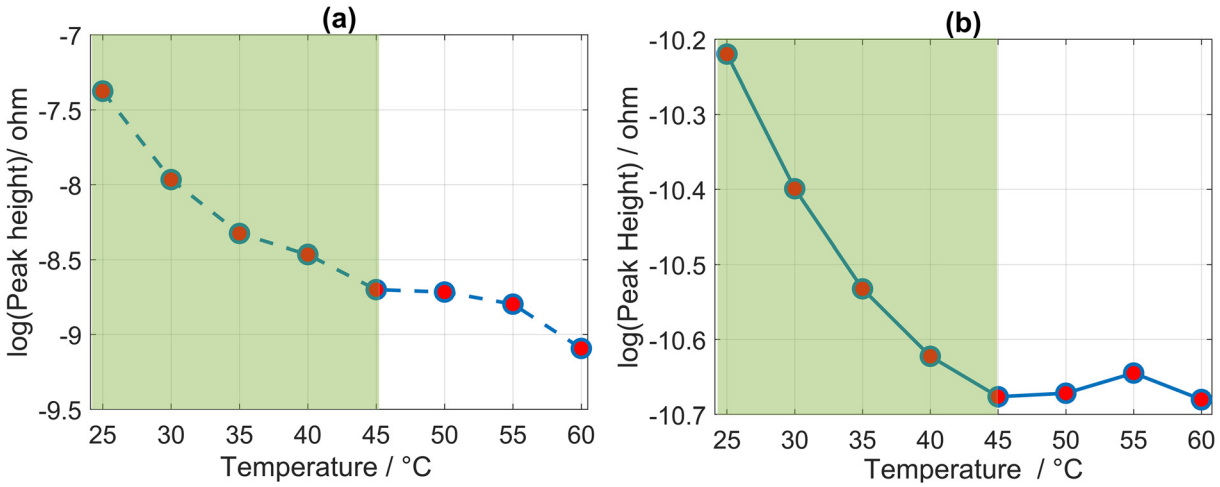

Fig. 4 Arrhenius relation based on DRT peak heights over the whole temperature range, indicating multiple linear regions at SOC 70, (a) cylindrical cell, (b) pouch cell.

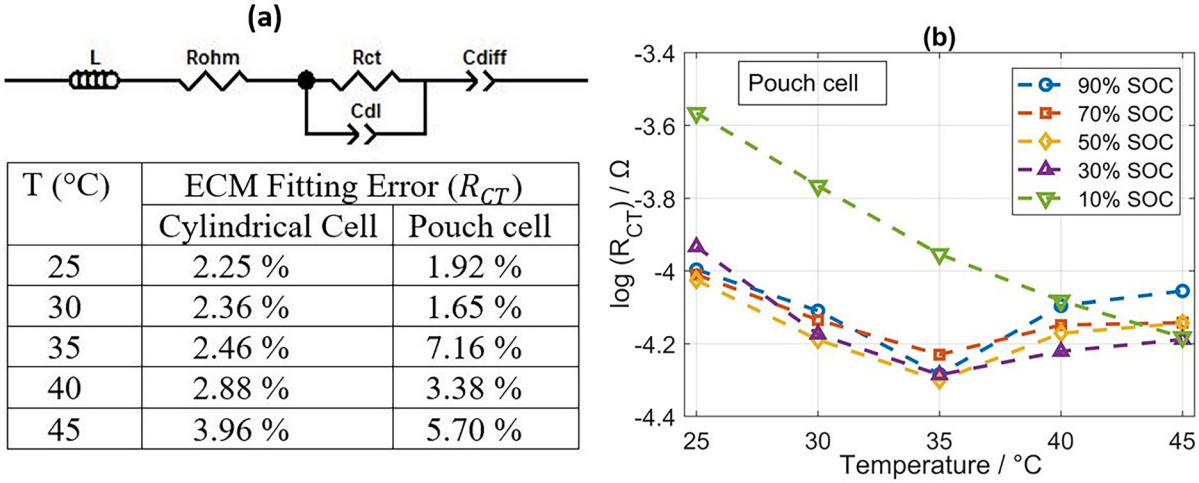

T (°C)	ECM Fitting Error (R_{CT})	
	Cylindrical Cell	Pouch cell
25	2.25 %	1.92 %
30	2.36 %	1.65 %
35	2.46 %	7.16 %
40	2.88 %	3.38 %
45	3.96 %	5.70 %

Fig. 5 (a) ECM with fitting errors at 70% SOC for both cells to extract R_{CT}, (b) Arrhenius relation for pouch cells R_{CT} extracted from ECM under multiple SOCs.

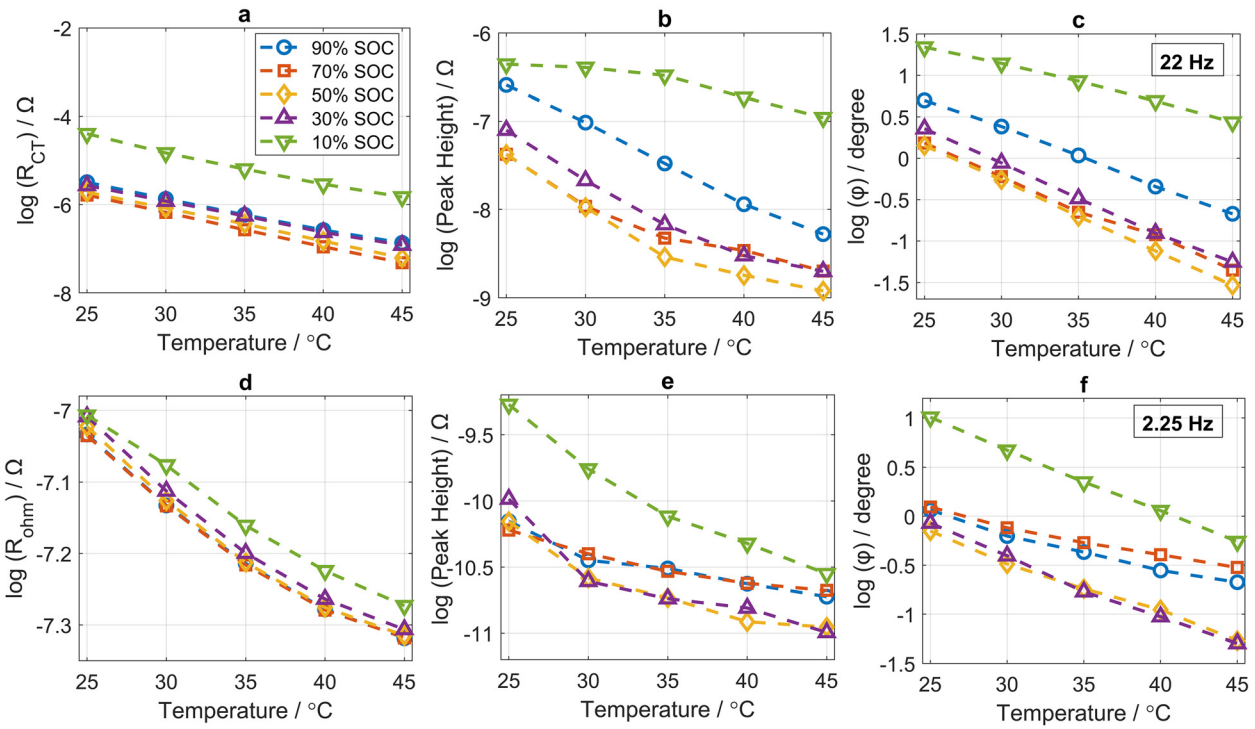

Fig. 6 Arrhenius relation for all three extracted features for both cell types at multiple SOCs. (a) RCT (cylindrical cell), (b) DRT peak height (cylindrical cell), (c) phase shift at 22 Hz (cylindrical cell), (d) R_{ohm} (pouch cell), (e) DRT peak height (pouch), (f) phase shift at 2.2 Hz (pouch).

increase in fitting errors for pouch cells with increasing temperature as compared to cylindrical cells (see Fig. 5(a)). This higher inaccuracy for pouch cells could be attributed to the influence of high-frequency inductive tail and its masking effect on the charge transfer arc. Therefore, a poor signal-to-noise ratio was observed, particularly for low impedance pouch cells. Since the variation in the zero-crossing will depend only on changes in ohmic resistance, given that the inductive effects should be constant. As a result, we have chosen internal resistance (R_{ohm}) for pouch cells to infer battery temperature. The resistance values were extracted from the zero-crossing (where $Z_{imaj} = 0$), and a linear Arrhenius relation was built as shown in Fig. 6(d).

Arrhenius relation was established over all SOCs using R_{CT}/R_{ohm}, DRT peak height and φ to illustrate a comprehensive temperature sensitivity as shown in Fig. 6. The top row rep-

resents cylindrical cells, while the bottom row corresponds to pouch cells. It is evident that all features exhibit high-temperature dependence, whereas dependence on SOC remains minimal. Therefore, the impact of SOC on temperature estimation in this study could be neglected. As discussed earlier, due to faster kinetics, both R_{CT}/R_{ohm} and DRT peak heights exhibited a decreasing monotonic trend with an increase in temperature for both cell types (see Fig. 6(a, b, d and e)). Both peaks for pouch and cylindrical cells showed almost identical behaviour. These peaks are likely associated with charge transfer processes, exhibiting a strong Arrhenius relation and provide good candidate features for temperature estimation based on DRT for both cell types.

A similar conclusion was also made by Chen *et al.*,[45] who attributed the peak with temperature dependence to charge transfer processes. This could also be translated for phase-based Arrhenius relations for both cell types (see Fig. 6(c and f)). Phase shift (φ) quantifies the degree of reactive/capacitive behavior at any given frequency. With a reduction in φ, the battery system's response is more dominated by resistive components and less by reactive (capacitive and inductive) components, as the phase shift approaches zero. As an example, for cylindrical cells at 22 Hz, the actual phase value is −1.20° and −0.26° for 25 °C and 45 °C, respectively, as also depicted in Fig. 3(a) (encircled). Increasing temperature leads to faster kinetics and diffusion processes, which reduces time constants for these processes and shifts the impedance at any given frequency downwards, thus any reduction in imaginary impedance will lead to a decrease in φ.[23,25,31]

3.3. Prediction model and validation

In order to estimate the accuracy of temperature estimation derived from the aforementioned features, a model-based assessment was conducted in two stages. Firstly, linear Arrhenius fitting was performed using a single cell for both cell types, and then two more cells were validated based on the built model to assess method reliability. Each feature-based Arrhenius relation (as shown previously in Fig. 6) was modelled using the curve-fit tool in MATLAB for all SOCs. The experimental data were fitted using a 1st order polynomial equation, following the traditional Arrhenius equation. To evaluate the model's performance and compare the effectiveness of each feature for both cell types, the prediction is assessed quantitatively by root mean square error (RMSE/°C) and R^2 (a measure of variance in prediction) as shown in Table 2.

The fitting results summarized in Table 2 indicate that overall cylindrical cells exhibit lower estimation errors as compared to pouch cells. This suggests a robust prediction based on the extracted features over all tested SOCs. Slightly higher errors for pouch cells imply a less precise fit, potentially due to differences in the intrinsic impedance response for both cell types. Also, the deviation of errors (for both cell types) between all SOCs is not significant, which suggests a minimal influence of SOC on temperature estimation for the proposed method. Generally, the model represents a good fit and can fit

Table 2 Model prediction performance based on RMSE (°C) and R^2 for both cell types under multiple SOCs

	Cylindrical cell					Pouch cell				
	RMSE (°C) & (R^2)					RMSE (°C) & (R^2)				
	SOCs					SOCs				
Model feature	10%	30%	50%	70%	90%	10%	30%	50%	70%	90%
DRT	2.69 (0.91)	1.75 (0.96)	2.40 (0.93)	2.41 (0.93)	0.46 (0.99)	1.7 (0.96)	3.7 (0.83)	2.9 (0.89)	1.95 (0.95)	2.56 (0.92)
Phase	0.50 (0.997)	0.33 (0.998)	0.12 (0.999)	0.60 (0.995)	0.25 (0.999)	0.22 (0.999)	0.67 (0.994)	0.67 (0.994)	1.06 (0.986)	1.21 (0.98)
R_{CT}/R_{ohm}	0.68 (0.994)	0.32 (0.99)	0.17 (0.999)	0.15 (0.997)	0.43 (0.997)	0.83 (0.992)	1.48 (0.973)	1.57 (0.97)	1.49 (0.97)	1.44 (0.97)

the experimental data as almost all values for R^2 are ~>0.9. For both cell types, among all three features, the DRT peak exhibits higher errors over all tested SOCs.

Furthermore, the fitting accuracy can be improved by applying a polynomial equation of higher degree, *i.e.*, second-order polynomial. In real-world scenarios, the relation between the proposed features and temperature is not strictly Arrhenius (linear); therefore, a higher-order term could capture the deviations from linearity. As an example, in our case for pouch cells (using DRT peak), upon utilizing a 2nd order polynomial equation the estimation errors were improved to lower values, *i.e.*, 0.46 °C, 1.87 °C, 1.59 °C, 0.81 °C and 1.35 °C for SOCs 10%, 30%, 50%, 70% and 90% respectively. This is also in agreement with other studies that used a higher-order fitting and claimed improved accuracy.[28,46]

While higher-order fitting improves the prediction accuracy, the focus of our study is not on optimizing Arrhenius fitting, but rather on comparing various temperature estimation methods *via* impedance features on different cell types, particularly a perspective on using DRT as a novel approach. Therefore, we maintain the traditional Arrhenius fitting approach to build the prediction model. Moreover, on average, for cylindrical cells, the fitting estimation is 1.92 °C, 0.36 °C and 0.35 °C for DRT peak, phase, and R_{CT} respectively, whereas it is 2.56 °C, 0.76 °C and 1.36 °C for DRT peak, phase, and R_{ohm} for pouch cells (see Table 2). It can be argued that for both cell types, the range of estimation accuracy is satisfactory, as it remains within the rated measurement accuracy of ±2.2 °C for most commercial thermocouples.[47]

Further analysis was performed by validating the Arrhenius model using the data from reference cells for cylindrical and pouch cells, as shown in Fig. 7. The validation results are categorised into two sets, *i.e.*, a set comprising of cell numbers 1 and 2 corresponds to cylindrical cells and another set of cell numbers 3 and 4 relates to pouch cells.

In the case of the high-energy, cylindrical cells, it can be concluded that among all three features, R_{CT} performed well and managed to estimate temperature with the lowest RMSEs, *i.e.*, on average the errors are in the range of 0.21 °C to 0.84 °C. Whereas, slightly higher errors were observed for the other two features, *i.e.*, an error range of 0.44 °C to 2.25 °C and 0.46 °C to 1.19 °C can be noticed for DRT peaks and phase, respectively (see cell 1 and 2 in Fig. 7). On the contrary, higher estimation errors were observed for pouch cells over all the features as compared to cylindrical cells (see cell 3 and 4 in Fig. 7). Here, the prediction performance for both DRT peak

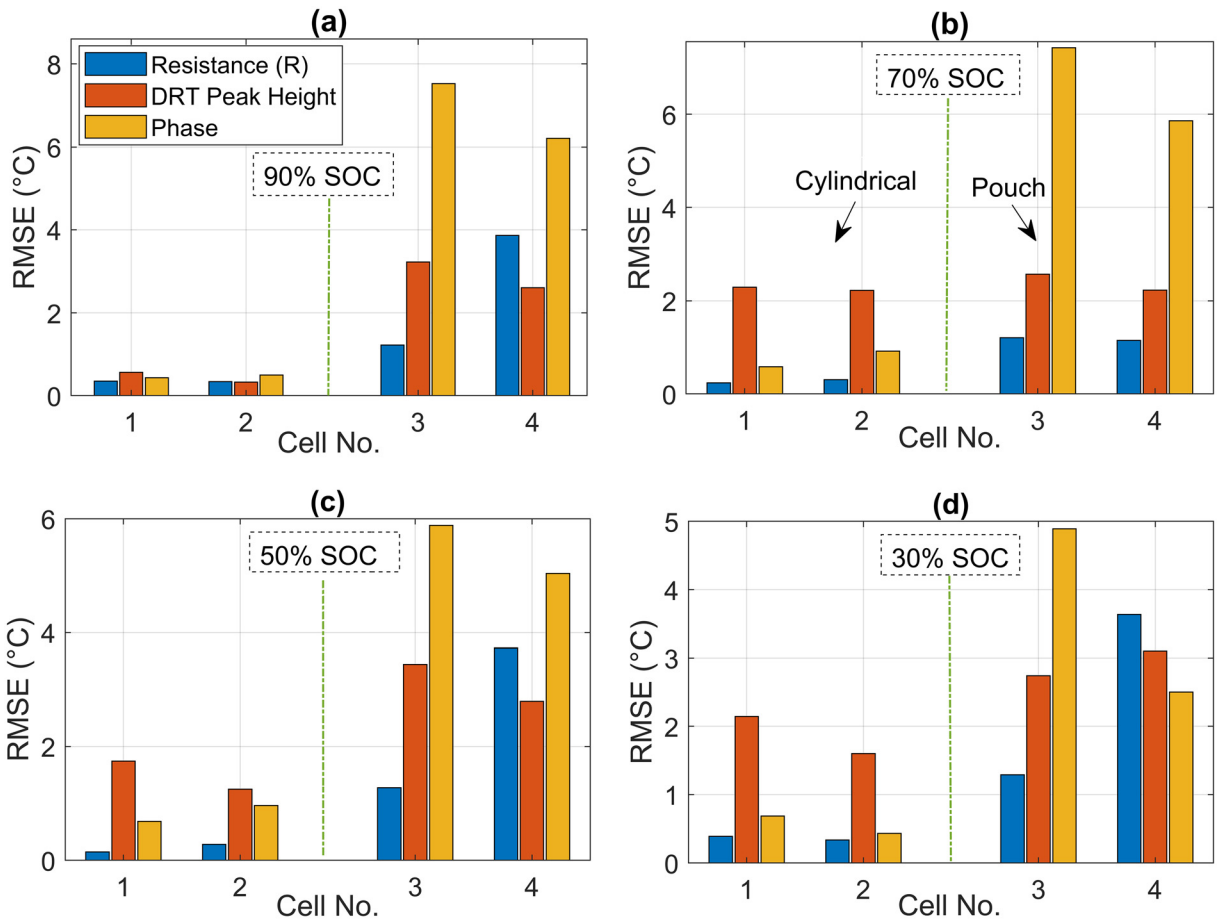

Fig. 7 Model validation using Arrhenius fit and RMSE (°C) based comparison of proposed impedance features at multiple SOCs for both cell types, (a) validation at 90% SOC, (b) 70% SOC, (c) 50% SOC, and (d) 30% SOC.

and R_{ohm} were observed to be in the almost similar range of 1.5 °C to 3 °C and 1.2 °C to 2.5 °C respectively.

Even though model fitting results for phase showed a good approximation for pouch cells (see Table 2), validation of this model revealed that this particular feature faced difficulty in providing low errors compared to cylindrical cells. Higher estimation errors of 2.23 °C to 6.86 °C were observed when using phase for pouch cells. Higher cell–cell variability and poor impedance measurement accuracy of low-impedance cells may contribute to worse phase-based temperature estimation. These findings indicate that, despite phase being used as a temperature predictor in previous studies, its applicability among cells with very low impedance should be considered carefully.

Interestingly, a similar level of errors can be noticed for the DRT peak method for both pouch and cylindrical cell at 70% SOC as shown in Fig. 7(b), where DRT performed consistently regardless of the cell type and estimated the temperature with an RMSE of <2.3 °C. Overall among all investigated SOCs, R_{ohm} and R_{CT} stands out with the lowest prediction errors of 2.22 °C and 0.41 °C for pouch and cylindrical cells respectively. This was followed by errors of 2.56 °C and 5.138 °C for DRT and phase respectively for pouch cells. Similarly, the estimation errors were 1.63 °C and 0.76 °C for DRT and phase respectively for cylindrical cells. Specifically for the proposed temperature estimation methodology, it can be concluded that leveraging the DRT feature, by utilising the selected peaks for both cell types, temperature can be estimated with a maximum error of <3 °C over the whole range of SOCs.

Although the temperature estimation in this study yielded adequate results, the method still suffers from a number of challenges. Herein, proposed analytical methods require a lookup table or empirical fit for temperature correlation. Due to their open-loop nature, to maintain accuracy, the model parameters need to be updated if to account for changes related to ageing. Impedance measurements tend to converge at elevated temperatures, resulting in poor estimation at elevated operating conditions. As highlighted in this study, the method accuracy has a particular limitation when applied to low impedance cells. This results in need for extensive preliminary tests for accurate estimation. Furthermore, impedance-based estimation gives an approximation of volume-averaged temperature, which is inclusive of the cell core temperatures otherwise ignored in surface-based measurements, but potentially underestimates localised hotspots. While machine learning could be utilised to bypass the requirement of explicit parameter estimation, it requires a substantially large dataset for reliable performance. It is important to consider these limitations in future studies to enhance the wider applicability of the method described herein.

4. Conclusion

This study successfully utilises a non-destructive sensor-less approach of leveraging EIS and DRT to infer battery temperature. An Arrhenius fit model based on extracted impedance features in the temperature range of 25 °C to 45 °C was performed on two cell types with different ranges of impedance, *i.e.*, high energy (5 Ah cylindrical) and high power (40 Ah pouch) cells. The proposed methods exhibit good accuracy for the evaluated cylindrical cell, whereas achieving high accuracy when applied to the low-impedance pouch cells seems more challenging. This can be attributed to poor signal-to-noise ratio for a low impedance system, particularly under high temperature operating conditions.

Three distinct features were extracted for comparison from EIS data, *i.e.*, R_{CT}/R_{ohm} (from ECM), DRT peak heights and phase shift (from raw data). DRT was proven to have an advantage over ECM-based interpretation due to its model-independent nature. DRT managed to effectively separate the overlapping distinct electrochemical processes, thus facilitating identification of the temperature sensitive peaks. To build an DRT based Arrhenius relation, two distinct DRT peaks C2 and D2 were selected for cylindrical and pouch cells respectively. Two peak properties analyzed, shift in time-constant and reduction of height with increasing temperature, can be attributed to faster electrochemical kinetics.

Through cross-validation of the Arrhenius fit with reference cells, it was concluded that R_{CT} (cylindrical) and R_{ohm} (pouch) outperforms other features by yielding the lowest estimation errors of 0.41 °C and 2.22 °C, respectively. Following, DRT peaks exhibited errors of 1.63 °C and 2.56 °C for cylindrical and pouch cells, respectively. Importantly, it was noticed that the useful detectable range for phase-temperature sensitivity for pouch cells is much smaller than cylindrical cells, therefore, a comparatively high validation error of 5.13 °C was observed for pouch cells as opposed to better performance of cylindrical cells model with an error of 0.76 °C.

In summary, this study considers the method of sensor-less thermal estimation with promising accuracy, and highlights two main challenges *i.e.*, the accuracy decrease when applied to very low impedance cells, and feature-temperature correlation becoming non-linear over higher temperature ranges. If solely relying on traditional Arrhenius fit, there should be a consideration of applying secondary fit to account for multiple activation energies for temperatures above 45 °C. As impedance of cells tends to converge with increasing temperature, accurate EIS measurements are crucial to selecting the optimal features. Future work should be directed towards universality of this method over different battery formats and chemistries, or adapting to select features insensitive to battery's state of health for ageing studies.

Author contributions

Danial Sarwar: Methodology, investigation, data curation, formal analysis, writing – original draft, conceptualization, experimentation. Oliver Curnick: Writing – review and editing, supervision, methodology. Tazdin Amietszajew: Writing – review & editing, supervision, funding acquisition, data curation.

Conflicts of interest

The authors declare that they have no known competing financial interests or personal relationships that could have appeared to influence the work reported in this paper.

Data availability

The data underpinning this publication will be available from Coventry University's open access repository, Pure, at **https://doi.org/10.57955/e19e4201-ba28-4508-8be1-f556c51385e8** from 01/10/2025 onwards, following the cessation of the embargo period.

Acknowledgements

The research work presented in this article is financially supported by the European Union's Horizon Europe project ENERGETIC (Grant No 101103667). 'This grant is covered under the UKRI Horizon Europe guarantee, Project reference number: 10069742. Views and opinions expressed are however, those of the author(s) only and do not necessarily reflect those of the European Union or CINEA.

References

1 Y. Zheng, Y. Che, X. Hu, X. Sui, D. I. Stroe and R. Teodorescu, *Prog. Energy Combust. Sci.*, 2024, **100**, 101120.
2 L. H. J. Raijmakers, D. L. Danilov, J. P. M. Van Lammeren, T. J. G. Lammers, H. J. Bergveld and P. H. L. Notten, *IEEE Trans. Ind. Electron.*, 2016, **63**, 3168–3178.
3 D. Li, L. Wang, C. Duan, Q. Li and K. Wang, *Int. J. Energy Res.*, 2022, **46**, 10372–10388.
4 R. Xiong, Y. Pan, W. Shen, H. Li and F. Sun, *Renewable Sustainable Energy Rev.*, 2020, **131**, 110048.
5 X. Feng, S. Zheng, D. Ren, X. He, L. Wang, H. Cui, X. Liu, C. Jin, F. Zhang, C. Xu, H. Hsu, S. Gao, T. Chen, Y. Li, T. Wang, H. Wang, M. Li and M. Ouyang, *Appl. Energy*, 2019, **246**, 53–64.
6 Y. Zhao, Y. Patel, I. A. Hunt, K. M. Kareh, A. A. Holland, C. Korte, J. P. Dear, Y. Yue and G. J. Offer, *J. Energy Storage*, 2017, **13**, 296–303.
7 S. Ma, M. Jiang, P. Tao, C. Song, J. Wu, J. Wang, T. Deng and W. Shang, *Prog. Nat. Sci.: Mater. Int.*, 2018, **28**, 653–666.
8 A. Soto, A. Berrueta, I. Oficialdegui, P. Sanchis and A. Ursúa, *IEEE Trans. Ind. Appl.*, 2022, **58**(2), 2400–2410.
9 M. Koseoglou, E. Tsioumas, D. Ferentinou, N. Jabbour, D. Papagiannis and C. Mademlis, *J. Power Sources*, 2021, **512**, 230508.
10 J. Fleming, T. Amietszajew, J. Charmet, A. J. Roberts, D. Greenwood and R. Bhagat, *J. Energy Storage*, 2019, **22**, 36–43.
11 T. Amietszajew, J. Fleming, A. J. Roberts, W. D. Widanage, D. Greenwood, M. D. R. Kok, M. Pham, D. J. L. Brett, P. R. Shearing and R. Bhagat, *Batteries Supercaps*, 2019, **2**, 934–940.
12 T. Amietszajew, E. McTurk, J. Fleming and R. Bhagat, *Electrochim. Acta*, 2018, **263**, 346–352.
13 C. Y. Lee, S. J. Lee, M. S. Tang and P. C. Chen, *Sensors*, 2011, **11**, 9942–9950.
14 C. M. Jones, M. Sudarshan, R. E. García and V. Tomar, *Sci. Rep.*, 2023, **13**, 1–11.
15 E. McTurk, T. Amietszajew, J. Fleming and R. Bhagat, *J. Power Sources*, 2018, **379**, 309–316.
16 Y. Yu, T. Vincent, J. Sansom, D. Greenwood and J. Marco, *J. Energy Storage*, 2022, **50**, 104291.
17 H. Zhang, X. Zhang, W. Wang and P. Yu, *Sensors*, 2023, **23**(11), DOI: **10.3390/S23115049**.
18 A. Jinasena, L. Spitthoff, M. S. Wahl, J. J. Lamb, P. R. Shearing, A. H. Strømman and O. S. Burheim, *Front. Chem. Eng.*, 2022, **4**, 804704.
19 G. Zhang, L. Cao, S. Ge, C.-Y. Wang, C. E. Shaffer and C. D. Rahn, *J. Electrochem. Soc.*, 2014, **161**, A1499–A1507.
20 General Motors, Cooling fins help keep Chevrolet Volt battery at ideal temperature, **https://phys.org/news/2011-02-cooling-fins-chevrolet-volt-battery.html**, (accessed 14 March 2025).
21 X. Lin, H. E. Perez, J. B. Siegel and A. G. Stefanopoulou, *IEEE Trans. Control Syst. Technol.*, 2020, **28**, 753–765.
22 O. J. Curnick, J. E. H. Sansom, J. Harper, M. Tsiamtsouri, R. Bhagat and D. Greenwood, *ECS Meet. Abstr.*, 2019, MA2019-02, 53.
23 R. Srinivasan, B. G. Carkhuff, M. H. Butler and A. C. Baisden, *Electrochim. Acta*, 2011, **56**, 6198–6204.
24 R. R. Richardson and D. A. Howey, *IEEE Trans. Sustainable Energy*, 2015, **6**, 1190–1199.
25 L. Wang, D. Lu, M. Song, X. Zhao and G. Li, *Int. J. Energy Res.*, 2020, **44**, 3082–3097.
26 L. H. J. Raijmakers, D. L. Danilov, J. P. M. Van Lammeren, M. J. G. Lammers and P. H. L. Notten, *J. Power Sources*, 2014, **247**, 539–544.
27 H. Beelen, K. Mundaragi Shivakumar, L. Raijmakers, M. C. F. Donkers and H. J. Bergveld, *Int. J. Energy Res.*, 2020, **44**, 2889–2908.
28 Y. Zheng, N. A. Weinreich, A. Kulkarni, Y. Che, H. Sorouri, X. Sui and R. Teodorescu, *25th European Conference on Power Electronics and Applications (EPE'23 ECCE Europe). IEEE*, 2023, 1–8.
29 N. S. Spinner, C. T. Love, S. L. Rose-Pehrsson and S. G. Tuttle, *Electrochim. Acta*, 2015, **174**, 488–493.
30 M. Kemeny, P. Ondrejka, D. Sismisova and M. Mikolasek, *J. Energy Storage*, 2024, **104**, 114566.
31 R. Schwarz, K. Semmler, M. Wenger, V. R. H. Lorentz and M. Marz, *IECON* 2015 – *41st Annu. Conf. IEEE Ind. Electron. Soc.*, 2015, 1536–1541.
32 J. P. Schmidt, S. Arnold, A. Loges, D. Werner, T. Wetzel and E. Ivers-Tiffée, *J. Power Sources*, 2013, **243**, 110–117.

33 F. Wenjie, Z. Zhibin, D. Ming and R. Ming, 2021 *Electr. Insul. Conf. EIC* 2021, 2021, 247–251.
34 J. Illig, J. P. Schmidt, M. Weiss, A. Weber and E. Ivers-Tiffée, *J. Power Sources*, 2013, **239**, 670–679.
35 M. Hahn, S. Schindler, L.-C. C. Triebs and M. A. Danzer, *Batteries*, 2019, **5**, 43.
36 F. Katzer and M. A. Danzer, *J. Power Sources*, 2021, **503**, 230009.
37 P. Shafiei Sabet and D. U. Sauer, *J. Power Sources*, 2019, **425**, 121–129.
38 Q. Zhang, D. Wang, E. Schaltz, D. I. Stroe, A. Gismero and B. Yang, *J. Energy Storage*, 2022, **55**, 105386.
39 T. H. Wan, M. Saccoccio, C. Chen and F. Ciucci, *Electrochim. Acta*, 2015, **184**, 483–499.
40 R. Lithium and I. Battery, *Build. Res. Inf.*, 1993, **21**, 21–22.
41 P. Specification.
42 A. Shabayek, A. Rathinam, M. Ruthven and D. Aouada, *J. Power Sources*, 2025, **629**, 235982.
43 P. Iurilli, C. Brivio and V. Wood, *Energy Technol.*, 2022, 2200547.
44 S. A. Inc, *Scribner Associates Inc.*, 2024, **https://www.scribner.com/software/68-general-electrochemistr376-zview-for-windows/**.
45 X. Chen, Q. Li, B. Shao, W. Dou, C. Lai and T. Lu, *Energy*, 2025, **320**, 135493.
46 R. R. Richardson, P. T. Ireland and D. A. Howey, *J. Power Sources*, 2014, **265**, 254–261.
47 O. Engineering, Thermocouple types, **https://www.dwyeromega.com/en-us/resources/thermocouple-types**, (accessed 2 April 2025).